Supporting Information

Mentes et al. 10.1073/pnas.1718316115

SI Materials and Methods

Cryo-EM Sample Preparation. Actin, calmodulin, and myo1b containing the motor domain and the IQ motif of the lever arm helix with bound calmodulin, containing a C-terminal AviTag and FLAG tag, were expressed and purified as described (1–3). Fresh samples of F-actin and frozen aliquots of myo1b and calmodulin were prepared at the University of Pennsylvania and shipped to Yale University. The myo1b and calmodulin samples were thawed and centrifuged before sample preparation. F-actin with excess myo1b and calmodulin was briefly mixed and incubated before centrifugation at ~350,000 × *g* for 15 min at 4 °C. The resulting pellet was resuspended in a buffer containing 10 mM KCl, 10 mM Mops (pH 7), 1 mM $MgCl_2$, 1 mM EGTA, 1 mM DTT, and 1 µM calmodulin (KMg10 with calmodulin). The ADP sample resuspension buffer also included 1 mM K_2ADP and an additional 1 mM $MgCl_2$.

Samples were plunge-frozen on carbon grids (Quantifoil R1.2/1.3) by using a manual plunger device. The grids for the ADP samples were lightly glow-discharged (10 s, 15 mA), while no glow discharge was used for the rigor samples. Samples were mixed with concentrated myo1b or resuspension buffer to optimize filament density and improve decoration based on the appearance of test grids analyzed on Yale University's 200-kV FEI-F20 electron microscope. The final ADP sample included ~6 µM F-actin, 14 µM myo1b, and 0.75 mM MgADP in KMg10 with calmodulin. The final rigor sample included ~7.5 µM F-actin and 17 µM myo1b in KMg10 with calmodulin.

Data Collection and Initial Processing. Micrographs were collected at Purdue University's cryo-EM facility with a 300-kV Titan Krios electron microscope equipped with a Gatan K2 Summit direct electron-counting camera. Automatic data collection was performed with Leginon (4). Micrographs were recorded with 55 subframes in 11-s exposures with a dose rate of ~4.7 $e\text{-}/Å^2{\cdot}s^{-1}$ over a defocus range of 0.8–2.8 µm. These images were collected in superresolution mode with a pixel size of 0.65 Å. In total, 660 micrographs were collected for the ADP sample, and 1,050 micrographs were collected for the rigor sample.

Micrographs were binned by two during movie alignment and dose correction in MotionCor2 (5). Subframe motion correction (where each movie frame was divided into smaller areas, or "patches," that were allowed to move separately; in this case, a 5 × 5 array was used) was applied to the ADP dataset micrographs, while whole-frame averaging was used for the rigor data. Contrast transfer function parameters were calculated by using Gctf (6). Particles were manually picked by using e2helixboxer from EMAN2 (7). A total of 76,000 particles were selected from 280 micrographs in the ADP dataset and 96,000 particles from 860 micrographs in the rigor dataset. Particles extracted from individual filaments were separated by the distance of one repeating subunit, ~27 Å.

The 3D Structure Refinement. Structure refinement was performed in RELION (Version 2.0.3) with helical processing (8, 9) by using a box size of 520 Å. Manually selected particles were fed directly into 3D refinement, with no intervening 2D classification step. A "full-particle" 3D soft mask, generated from an initial 3D reconstruction by the "relion_mask_create" tool, was utilized to eliminate noise in the solvent region of the reconstructed maps after each cycle of refinement. This procedure yielded maps with a global resolution of 3.9 Å for the ADP state and 5.4 Å for the rigor state. "Particle polishing" was applied to the rigor dataset, and the refinement was continued, although this step did not significantly affect the resolution of the map. Additional refinements were then performed by using the "unpolished" ADP data and the "polished" rigor data. In this latter step, a smaller soft mask (generated from the three central actin and myo1b subunits) was applied the reference volume after every cycle of refinement, to focus the refinement on the central region of the imaged filament segments, thus minimizing the tendency of bent filaments to introduce errors in the alignments. Soft masks were generated by fitting atomic models of actin and myo1b into each map, generating a 3D volume with pdb2mrc from the EMAN software suite (10), and then inputting these into the RELION mask creation tool. Following this procedure, the global resolution reached 3.2 Å in the ADP sample and 4.1 Å in the rigor sample.

Structural Classification. Particles were then sorted in two rounds of masked 3D classification in RELION. First, a soft mask representing a single central subunit from the filament was generated, by using the procedure described above; the resulting "central-subunit masks" were then subtracted from the full-particle soft masks utilized in the previous refinement steps, by using the relion_image_handler tool. The resulting "reverse" masks were applied to the refined 3D maps, and projections of the resulting volume were subtracted from the particle stacks to highlight the central actin and myo1b subunit. The 3D classification was then performed on these "subtracted" particle stacks, fixing the shift and orientation parameters obtained from the previous refinement. The ADP-state 3D classification was performed with 10 classes, yielding a dominant occupied class (corresponding to actomyosin) with 70% of particles (53,000) and an unoccupied class (corresponding to bare actin) with 25% of particles (19,000). The remaining 5% of particles, which were dispersed among the remaining eight classes, exhibited poorly resolved or artefactual density features and were discarded. The rigor-state 3D classification was performed with 14 classes, yielding a single occupied class with 84.6% of the particles (80,000) and a single unoccupied class with 14.4% of the particles (14,000). The remaining 2% of particles (dispersed among the 12 other classes) were discarded. Particles corresponding to occupied classes were restored to the "unsubtracted" state before initiating a new round of refinement, applying the full-particle mask in the first cycle and continuing with a three-subunit reference-volume mask generated by using the procedure described above. Following this classification procedure, the relative density of the central myosin subunit in the occupied class increased with respect to actin (reflecting increased occupancy), although there were no significant changes in resolution.

A second round of particle subtraction and 3D classification was then performed, by utilizing the above procedure but substituting Protein Data Bank (PDB) models of the N-terminal subdomain, lever arm, and light chain in place of the complete central subunit, to further focus the classification on conformational changes within myosin. The ADP-state 3D classification was performed with seven classes (again with fixed orientation and shift parameters), yielding a primary class (class A) with 75% of particles (40,000) and a secondary class (class B) with 14.6% of particles (7,700). The remaining 10% of particles, dispersed among the remaining five classes, exhibited poor resolution and/or weak density in the lever arm region (although consistent with the class A orientation) and were discarded. The rigor-state 3D classification was performed with 10 classes, yielding a class with 75.4% of the particles (60,000). The remaining 24.6% of particles were dispersed among the nine other classes, which included between 5.4% and 0% of particles; these classes were poorly resolved and hence discarded. All 3D classification steps in both rounds used references that were low-pass-filtered to 60 Å, a regularization parameter of $T = 2$, and a high-resolution limit of 6–8 Å. A final round of structure refinement was then performed for these classes, first with full-particle reference-volume masks and continuing with three-subunit masks as before. The final resolutions were 3.3 Å for ADP state A class, 3.7 Å for ADP state B, and 3.9 for the rigor state as calculated by postprocessing in RELION [Fourier shell correlation (FSC) = 0.143] using three-subunit soft masks (Figs. S3 and S4).

Resolution Estimation and Final Map Generation. Separate soft masks for the five central actin subunits together and the different subdomains of the central myo1b subunit were generated in RELION. These masks were used to calculate the resolution and b-factor of these regions separately in postprocessing with RELION (Fig. S2). Hybrid maps were generated for molecular dynamics flexible fitting (MDFF) calculations that included these regions filtered to their respective resolutions according to the FSC = 0.5 criterion or FSC = 0.143. Briefly, hybrid maps were generated by filtering the final map of a reconstruction to two different resolutions. A soft mask was applied to one of these filtered maps as normal, while the inverse mask was applied to the other filtered map. These masked maps were then summed together. As the same mask was applied to each filtered map, the overall cryo-EM density remained consistent throughout the resulting hybrid map. This process was iterated to add multiple separately filtered regions to the hybrid map (Fig. S3). Finally, a soft mask that included the central five actin subunits and the central myo1b subunits was applied as normal. These operations were performed in python.

Myo1b.Li_2SO_4 Crystallization and Structure Determination. Crystals of myo1b (10 mg/mL) in 10 mM Mops (pH 7.2), 50 mM KCl, 2 mM ADP, 2 mM MgCl, 1 mM DTT, and 1 mM EGTA were obtained at 4 °C by vapor diffusion in hanging drops by mixing 1.0 µL of protein solution and 1.0 µL of well solution [100 mM Mops (pH 7.0), 100 mM Li_2SO_4, and 10% PEG 3350]. Crystals belonging to the monoclinic P21 space group grew as clustered plates after ∼1 wk. For data collection, crystals were flash-frozen in liquid nitrogen from a cryosolution consisting of crystallization buffer supplemented with 11% PEG 1000 and 11% PEG 400. X-ray data collection was carried out at National Synchrotron Light Source beamline X25. Data were indexed and scaled by using HKL-2000 (HKL Research, Inc.) (11). Although the predicted crystal symmetry was nearly orthorhombic, the resulting unit cell was too small, with solvent content of ∼22%, to contain the protein. In addition, there was a clear twinning law (h, −k, −l) further suggesting that monoclinic is the correct symmetry assignment. The molecular replacement solution was found by using Phaser-MR in the program Phenix (12) with the crystal structure of apo-myo1b (PDB ID code 4L79) as the search model. The resultant model was refined by using Phenix with manual modifications done by using Coot (13). Final refinements were carried out alternately with Phenix. Although grown in the presence of MgCl and ADP, no nucleotide was observed in the active site of the crystalized protein. The statistics of the final Phenix-refined model are given in Table S1.

MDFF and MD Simulations.

Rigor model building. Flexible fitting was used to obtain atomic models for the ADP^A, ADP^B, and AM states. The starting model for AM was created by docking our myo1b.SO_4 structure (PDB ID code 5V7X), after computationally removing the SO_4 and a five-monomer high-resolution model of an actin filament (PDB ID code 3J8I; 5mer) into the AM cryo-EM electron density by using Chimera. The MDFF (14) plugin of NAMD (15) was then used to fit the starting model into our high-resolution (at FSC = 0.5 to minimize overfitting) density.

The VMD (16) plugin was first used to "Solvate" the protein with a transferable intermolecular potential with a 3-site water model. K^+ and Cl^- ions were added to neutralize the system and obtain a physiologically relevant ionic strength with "Autoionize." The "griddx" command from the MDFF package was used to convert the cryo-EM density maps from mrc format to dx format (the MDFF potential file). Subsequently, a PDB file containing the per-atom scaling factors was generated with "gridpdb." NAMD configuration files were generated by using the "mdff" setup command. The CHARMM27 force field (17) was used for the simulations. Periodic boundary conditions were used, along with a nonbonded interaction cutoff of 10 Å for particle Mesh Ewald long-range electrostatic interaction calculations. Bonds involving hydrogen atoms were constrained by using the SHAKE algorithm (18–22), allowing for a time step of 2 fs. Structures were saved every 10 ps.

A NAMD-suggested protocol, with some modifications, was used for the MD fit. Briefly, fitting of the proteins into the EM density started with low forces corresponding to $G = 0.01$ with increasing G at every 100 ps with increment of 0.01, up to higher forces ($G = 0.3$), for a total of 5 ns. The final structure at the end of MDFF simulations and the density map were then used for real space refinement and model building in COOT (13) and PHENIX (12). The final fitted rigor structure after MDFF simulations and Phenix real space refinement was used for structural analysis. The starting model built with crystal structure was relatively close to the final AM model, apart from rearrangements at the myosin–actin interface.

MgADP bound models. The starting models for ADP^A and ADP^B were created in slightly different ways. The ADP^A model was built by docking MgADP into the starting AM structure, and the ADP^B model was built by docking MgADP into the final MDFF rigor structure. In both cases the docking was carefully done by using the high-resolution Myo1c (PDB ID code 4BYF) (23) and MyoV (PDB ID code 1W7I) structures as templates to position the MgADP and coordinating residues. Following solvation and ionization, the positions of all waters in the MgADP bound models were energy minimized and thermally equilibrated while holding the positions of the MgADP and protein atoms fixed. The remaining MDFF and refinement steps were identical with the AM fit.

MD simulations of the MgADP-bound active site of AM.ADP^A. Residue E150 of myosin coordinated with the first water shell around the Mg atom during the MDFF of the AM.ADP^A structure. E150 is a highly conserved residue across the myosin superfamily that was not previously associated with a nucleotide interaction. Conventional MD simulations with no EM potential ($g = 0$) were consequently run eight times for an additional 4 ns after the fit to the check stability of the E150–water interaction. The transient interaction between the magnesium water shell and E150 was consistent for all eight MD simulations (Movie S5).

Definition of Myo1b Conformational Changes Using DynDom. DynDom (24) was used to identify subdomains of myo1b by comparing the structures of the ADP^A and AM states. The backbone root-mean-square deviation (rmsd) from a least-squares superposition of the two protein models must be >0.1 Å for the program to proceed. For each domain pair, the ratio of interdomain to intradomain displacement was set at 1.0 as suggested, and the minimum domain size was set at 20 residues. Three domains were identified by the program based on these parameters, and the domains were used to determine the interdomain screw axis and the bending regions. The program analyzes the interdomain motion for the pair of domains found and gives as output the screw axis orientation and the magnitude of translation and rotation of the moving domain relative to the fixed domain. Fig. S6 shows the domains found between ADP^A to AM states, where domain 1 (blue; N-terminal subdomain) comprises 143 residues, domain 2 (red; lever) comprises 119 residues, and domain 3 (yellow; motor) comprises 444 residues. Separately, calmodulin is shown in orange red and the N-terminal extension (residues 6–11) in magenta in Fig. S3. Rotations, translations, and bending/hinge residues of moving domains relative to a fixed domain defined by DynDom from $AM.ADP^A$ to AM state are summarized in Table S2.

Phalloidin Structure. The cryo-EM datasets contain regions of excess density at the interface of three actin monomers. We assume these densities represent phalloidin, the bicyclic heptapeptide [cyclic(L-Ala1-D-Thr2-L-Cys3-*cis*-4-hydroxy-Pro4-L-Ala5-2-mercapto-L-Trp6-4,5-dihydroxy-L-Leu7) cyclic (3->6) sulfide], which was used to stabilized the actin filaments. Of the available phalloidin structures (25–27), the one derived from NMR/MD of phalloidin in water at pH 3 (26) fits the densities with least modification. The phalloidin model was built with Chimera by using the published dihedral angles, then docked and fit into the density for $AM.ADP^A$ with MDFF. Following the fit, P4 and L7 were hydroxylated, and their torsions were adjusted manually with Chimera.

1. Laakso JM, Lewis JH, Shuman H, Ostap EM (2010) Control of myosin-I force sensing by alternative splicing. *Proc Natl Acad Sci USA* 107:698–702.
2. Shuman H, et al. (2014) A vertebrate myosin-I structure reveals unique insights into myosin mechanochemical tuning. *Proc Natl Acad Sci USA* 111:2116–2121.
3. Lin T, Tang N, Ostap EM (2005) Biochemical and motile properties of Myo1b splice isoforms. *J Biol Chem* 280:41562–41567.
4. Suloway C, et al. (2005) Automated molecular microscopy: The new Leginon system. *J Struct Biol* 151:41–60.
5. Zheng SQ, et al. (2017) MotionCor2: Anisotropic correction of beam-induced motion for improved cryo-electron microscopy. *Nat Methods* 14:331–332.
6. Zhang K (2016) Gctf: Real-time CTF determination and correction. *J Struct Biol* 193:1–12.
7. Tang G, et al. (2007) EMAN2: An extensible image processing suite for electron microscopy. *J Struct Biol* 157:38–46.
8. Scheres SH (2012) RELION: Implementation of a Bayesian approach to cryo-EM structure determination. *J Struct Biol* 180:519–530.
9. He S, Scheres SHW (2017) Helical reconstruction in RELION. *J Struct Biol* 198:163–176.
10. Ludtke SJ, Baldwin PR, Chiu W (1999) EMAN: Semiautomated software for high-resolution single-particle reconstructions. *J Struct Biol* 128:82–97.
11. Otwinowski Z, Minor W (1997) Processing of X-ray diffraction data collected in oscillation mode. *Methods Enzymol* 276:307–326.
12. Adams PD, et al. (2010) PHENIX: A comprehensive Python-based system for macromolecular structure solution. *Acta Crystallogr D Biol Crystallogr* 66:213–221.
13. Emsley P, Lohkamp B, Scott WG, Cowtan K (2010) Features and development of Coot. *Acta Crystallogr D Biol Crystallogr* 66:486–501.
14. Trabuco LG, Villa E, Mitra K, Frank J, Schulten K (2008) Flexible fitting of atomic structures into electron microscopy maps using molecular dynamics. *Structure* 16:673–683.
15. Phillips JC, et al. (2005) Scalable molecular dynamics with NAMD. *J Comput Chem* 26:1781–1802.
16. Humphrey W, Dalke A, Schulten K (1996) VMD: Visual molecular dynamics. *J Mol Graph* 14:33–38.
17. MacKerell AD, Jr, Banavali N, Foloppe N (2000–2001) Development and current status of the CHARMM force field for nucleic acids. *Biopolymers* 56:257–265.
18. Ryckaert J-P, Ciccotti G, Berendsen HJC (1997) Numerical integration of the Cartesian equations of motion of a system with constraints: Molecular dynamics of n-Alkanes. *J Comput Phys* 23:327–341.
19. Yoneya M, Berendsen HJC, Hirasawa K (1994) A noniterative matrix method for constraint molecular-dynamics simulations. *Mol Simul* 13:395–405.
20. Forester TR, Smith W (1998) SHAKE, rattle, and roll: Efficient constraint algorithms for linked rigid bodies. *J Comput Chem* 19:102–111.
21. McBride C, Wilson MR, Howard JAK (1998) Molecular dynamics simulations of liquid crystal phases using atomistic potentials. *Mol Phys* 93:955–964.
22. Andersen HC (1983) RATTLE: A "velocity" version of the SHAKE algorithm for molecular dynamics calculations. *J Comput Phys* 52:24–34.
23. Münnich S, Taft MH, Manstein DJ (2014) Crystal structure of human myosin 1c–The motor in GLUT4 exocytosis: Implications for Ca2+ regulation and 14-3-3 binding. *J Mol Biol* 426:2070–2081.
24. Hayward S, Kitao A, Berendsen HJ (1997) Model-free methods of analyzing domain motions in proteins from simulation: A comparison of normal mode analysis and molecular dynamics simulation of lysozyme. *Proteins* 27:425–437.
25. Kessler HWT (1991) Solution structure of phalloidin obtained by NMR spectroscopy in [D6]DMSO and molecular dynamics calculation in vacuo and in water. *Eur J Org Chem* 1991:179–184.
26. Kobayashi N, et al. (1995) Comparative study on the conformation of phalloidin, viroisin, and related derivatives in aqueous solution. *Eur J Biochem* 232:726–736.
27. Zanotti G, et al. (2001) Solid state and solution conformation of [Ala7]-phalloidin: A synthetic phallotoxin analogue. *Chemistry* 7:1479–1485.
28. Cardone G, Heymann JB, Steven AC (2013) One number does not fit all: Mapping local variations in resolution in cryo-EM reconstructions. *J Struct Biol* 184:226–236.
29. Wallace AC, Laskowski RA, Thornton JM (1995) LIGPLOT: A program to generate schematic diagrams of protein-ligand interactions. *Protein Eng* 8:127–134.

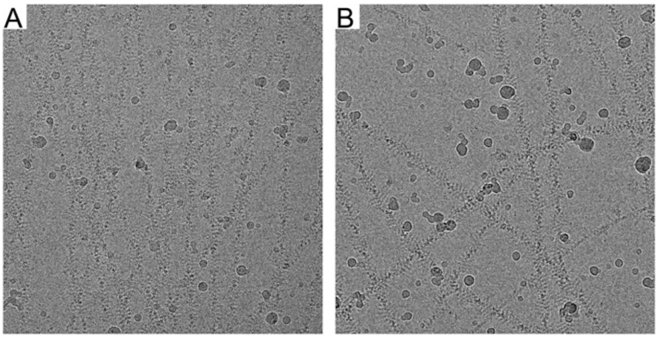

Fig. S1. Representative micrographs from the ADP (*A*) and rigor (*B*) datasets of myo1b-decorated actin filaments used for single-particle cryo-EM analysis. Micrograph dimensions are 7676 × 7420 pixels, with a pixel size of 0.65 Å.

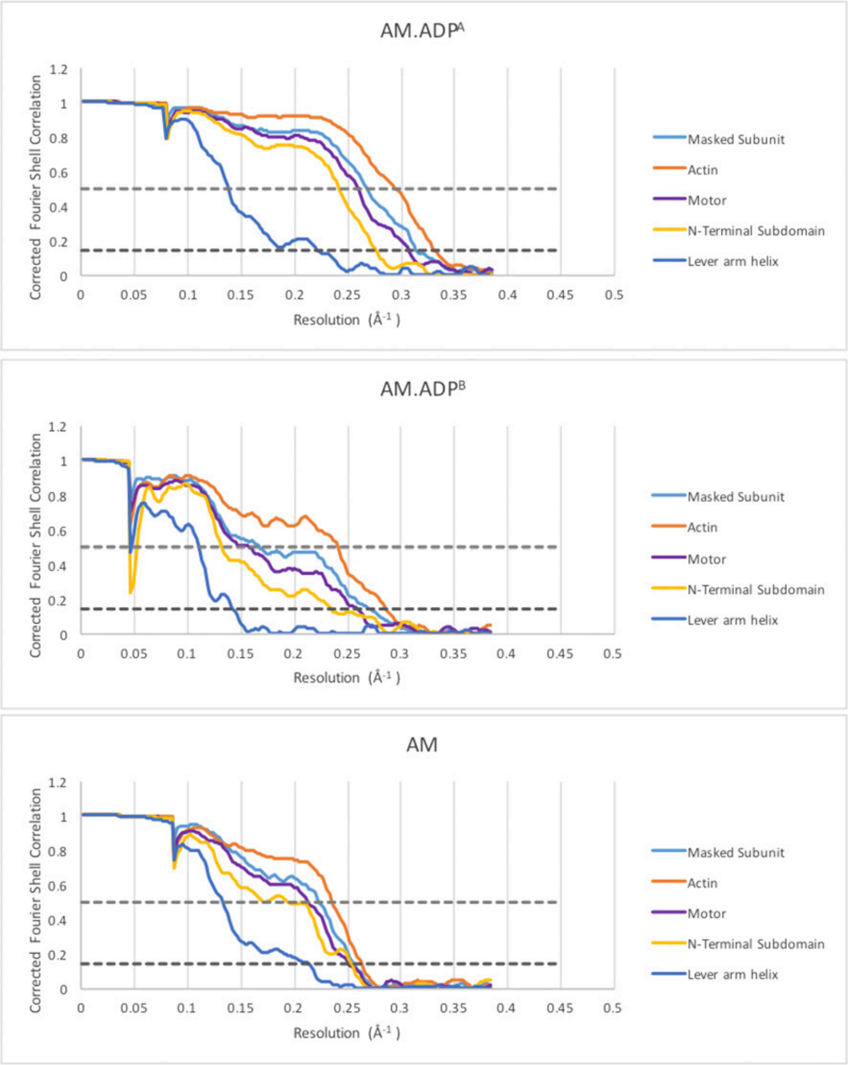

Fig. S2. Independently refined half-dataset maps were used in FSC calculations to estimate the resolution of different subregions. High-resolution noise substitution was used to correct the correlations for bias introduced by the masks. The masks were filtered to 20 Å and included a soft edge of 6–8 pixels (7.8–10.4 Å).

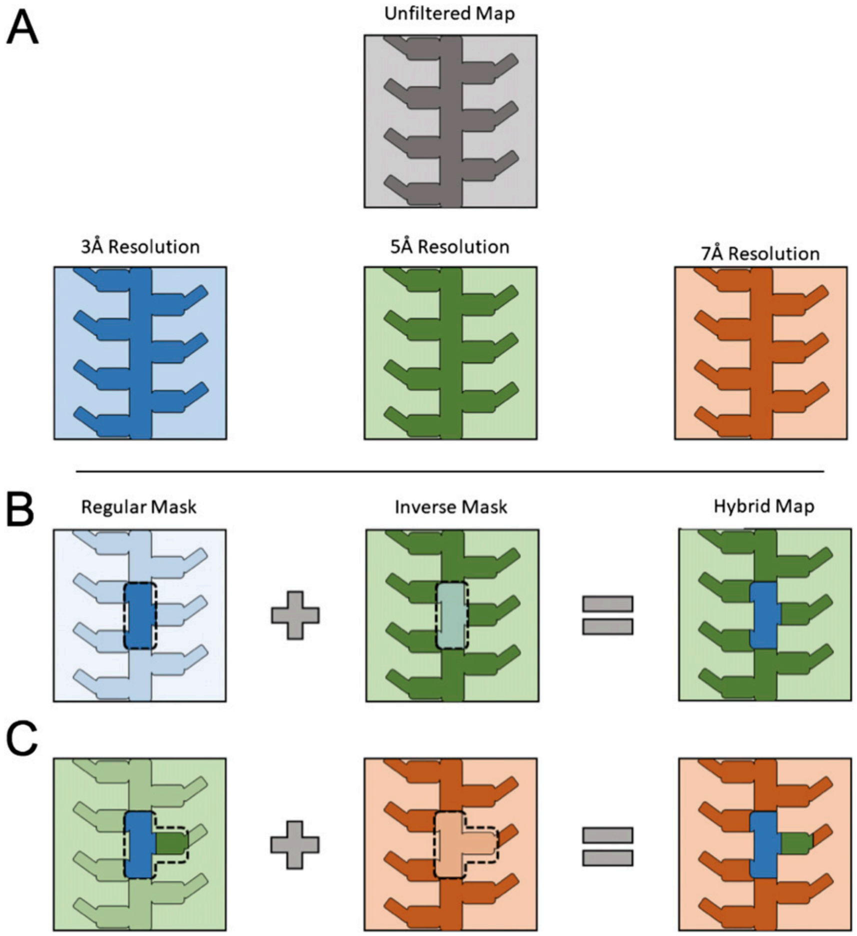

Fig. S3. Hybrid map construction. (*A*) Hybrid maps are generated by filtering a reconstructed volume to different resolutions. In this example, an original map (gray) is filtered to 3-, 5-, and 7-Å resolution (blue, green, and orange). (*B*) Next, a map is applied to one of these filtered maps as normal, while the inverse of the same mask is applied to a different filtered map. These masked maps are then added together to generate a hybrid map. (*C*) Next, the resulting hybrid map can be used in additional rounds of map hybridization to generate complex hybrid maps.

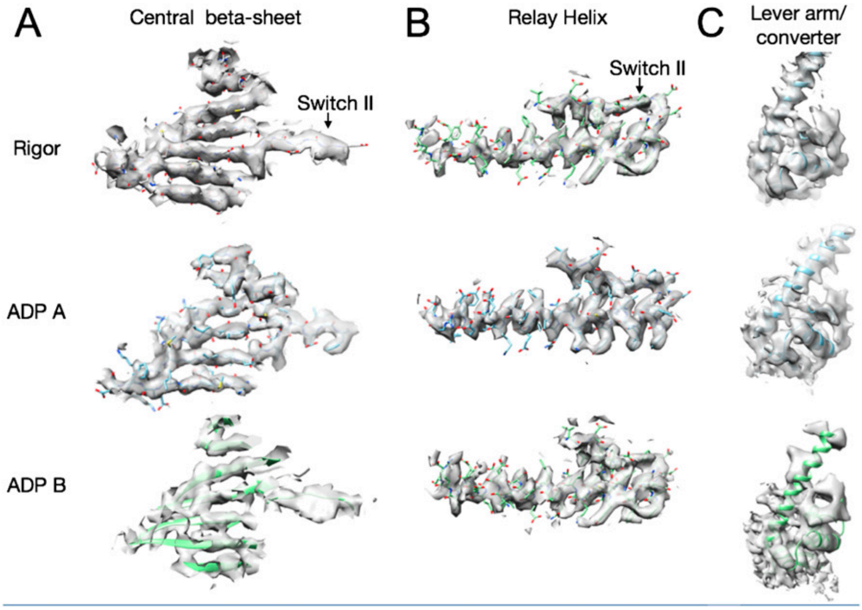

Fig. S4. Representative density elements within the motor domain. Selected features from the myosin motor domain were extracted from cryo-EM maps by using the "zone" feature of UCSF Chimera. (*A*) Central beta sheet. (*B*) Relay helix. (*C*) Lever arm/converter.

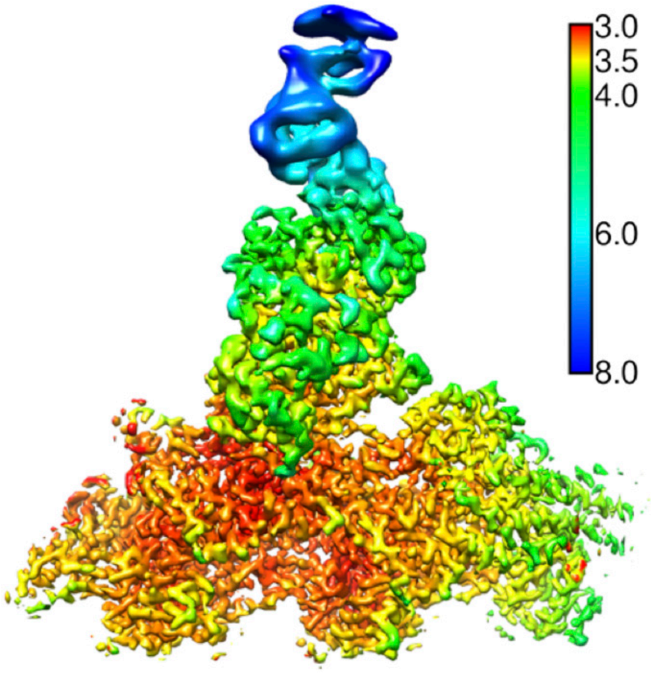

Fig. S5. Local resolution estimation shows progressively lower resolutions at higher radial distances. The program "blocres" (28) was used to produce voxel-wise estimates of the map resolution for the ADP^A map. The results of blocres were used to generate an adaptively filtered version of the original map ("blocfilt" function). The adaptively filtered map is depicted as an isosurface, colored according to the resolution estimates from blocres (see color key) by using the "Surface color" function of UCSF Chimera. Similar calculations applied to the ADP^B and rigor maps gave the same general trend of lowered resolution at larger radial distances from the filament axis. However, the ADP^B and rigor maps produced this way were evidently overfiltered, as reflected by the loss of side-chain features that are evident in Fig. S4; we attribute this effect to an overly stringent FSC cutoff criterion (FSC = 0.5) required for useful operation of blocres. As seen in Fig. S2, there is a gradual falloff of the FSC in these maps, so that a substantial portion of the curves lies below the more conservative 0.5 threshold, but remains above the less stringent 0.143 threshold (particularly for the ADP^B and rigor cases). Consequently, higher-resolution features that are noisy but interpretable (Fig. S4) are eliminated from the adaptively filtered maps.

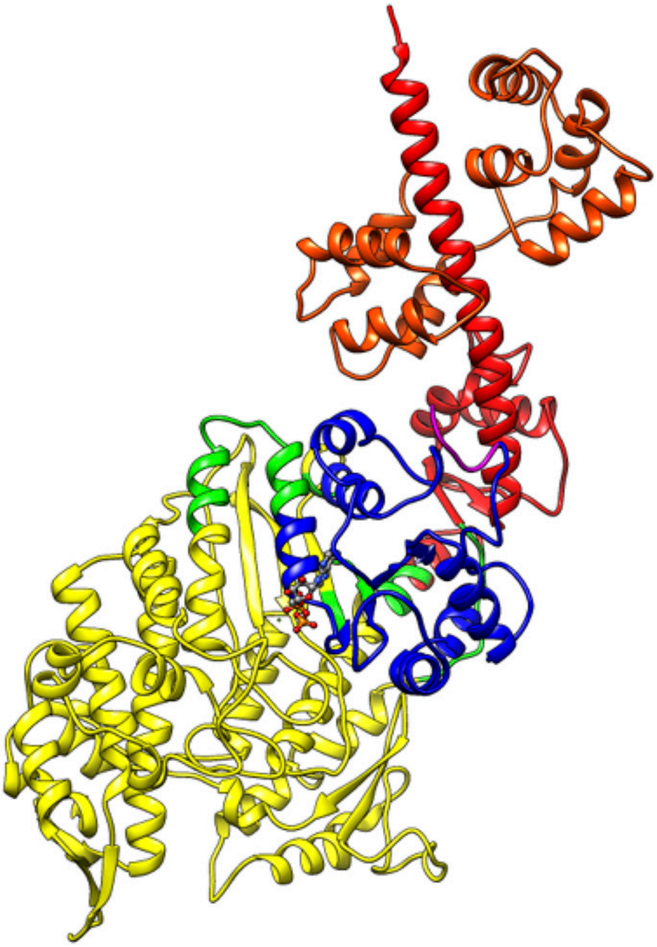

Fig. S6. Myo1b subdomains and bending residues defined by DynDom from AM.ADP^{A} to AM state. Motor (yellow), N-terminal subdomain (blue), lever (red), and bending and hinge residues (green) are defined in Table S2. The N-terminal extension residues (magenta) and calmodulin (orange-red) are shown.

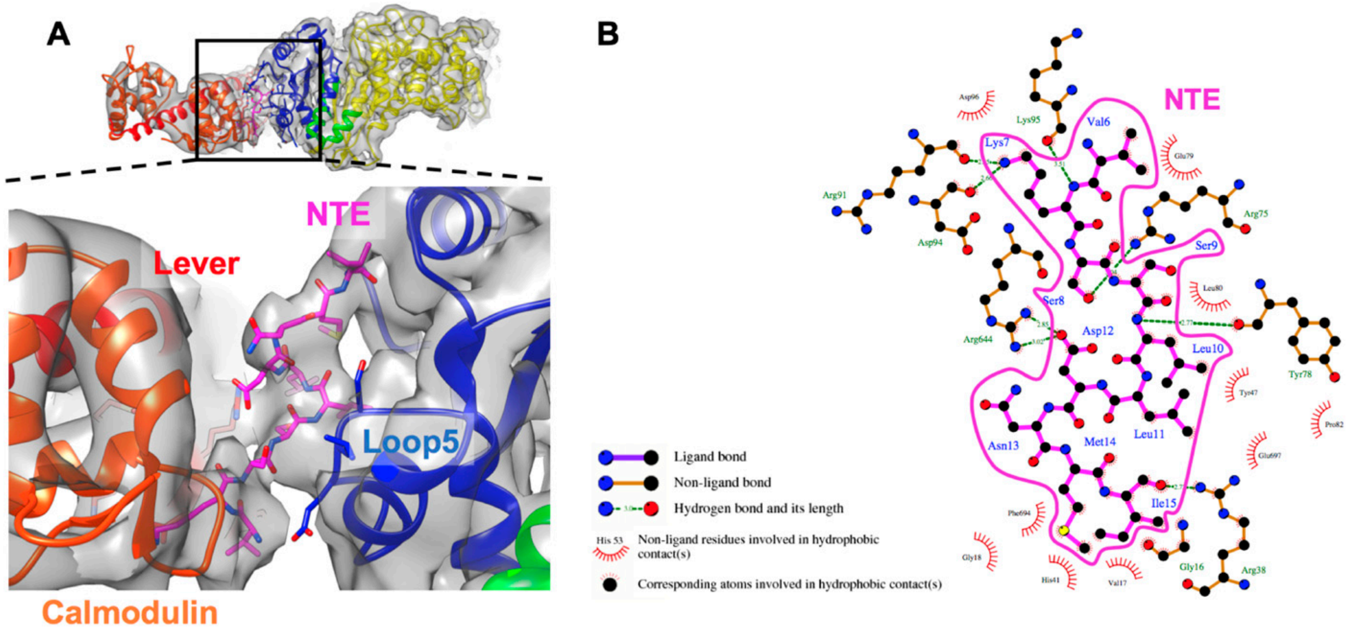

Fig. S7. Conformation of the N-terminal extension. (*A*) The N-terminal extension (6–15) in AM state shown with cryo-EM density map. The N-terminal extension residue side chains and side chains of surrounding residues of loop 5 (blue) and lever (red) are shown with stick representation. (*B*) The interaction of N-terminal extension (NTE) with surrounding residues in a 2D interaction map prepared with LigPlot (29). The side-chain interaction map was created by using the apo-myo1b crystal structure (PDB ID code 4L79) and is consistent with the lower-resolution cryo-EM map.

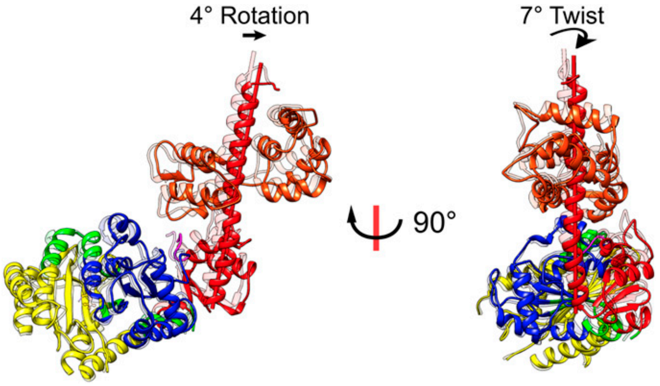

Fig. S8. Movement of the N-terminal subdomain results in the oblique rotation of the lever as it transitions from AM.ADP^B (transparent color) to AM (solid color) state. N-terminal subdomain (blue), lever (red), and calmodulin (orange-red). The lever arm rotates 4° and twists 7° from AM.ADP^B to AM, measured with respect to the motor domain. The oblique nature of this 4° rotation, compared with the much larger lever arm swing (24°) from AM.ADP^A to AM, means that the magnitude of the swing from AM.ADP^A to AM.ADP^B (25°) is nearly identical to the AM.ADP^A to AM transition.

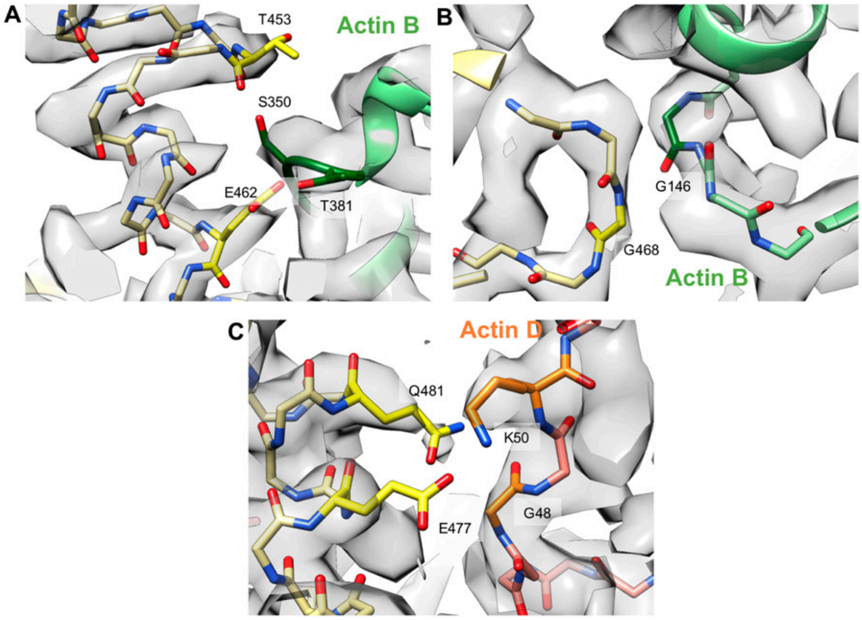

Fig. S9. Interaction of the myo1b activation loop and helix–loop–helix motif with two actin subunits. (*A*) Interaction of myosin E462 with S350 and T351 in actin (subunit B; green) and the myosin activation loop T453 interaction with S350 of actin. (*B*) Interaction of myosin G468 with actin G146 (subunit B; green). (*C*) Interactions between myosin E477 and the side chain of actin K50 (subunit D; orange); myosin Q481 side-chain oxygen with the backbone hydrogen of actin G48 (subunit D; orange).

Table S1. Structure data collection and refinement statistics

Data collection	
Space group	P 1 2_1 1
Cell dimensions	
a, b, c, Å	109.74, 48.73, 118.51
α, β, γ, °	90.00, 89.95, 90.00
Resolution, Å	40.00–3.15 (3.26–3.15)*
No. of unique reflections	22,362
$I/\sigma I$	11.9 (3.5)*
Completeness, %	98.7 (87.0)*
Redundancy	7.4 (7.1)
Twin operator	h, −k, −l
Twin fraction	0.40
Refinement	
Resolution, Å	39.504–3.141 (3.287–3.141)*
No. of unique reflections	22,155
No. of test reflections	1,101
$R_{\text{work}}/R_{\text{free}}$	0.1962/0.2184
No. of atoms	
Protein	6,976
Ligand/ion	5
Average B factors, Å^2	
Protein	39.5
Ligand/ion	25.5
rmsd	
Bond lengths, Å	0.004
Bond angles, °	0.678
MolProbity statistics	
Clash score	10.02
Rotamer outliers, %	2.35
Cβ outliers, %	0
Ramachandran plot	
Favored, %	96.12
Outliers, %	0

*Values for highest-resolution shell.

Table S2. **Rotations, translations and bending/hinge residues of moving domains relative to a fixed domain defined by DynDom from AM.ADP^{A} to AM state**

Fixed domain	Moving domain	Rotation angle, °	Translation, Å	Bending residues	Hinge residues
Nterm (blue)	Lever (red)	21	1.5	629–633	No mechanical hinges
Nterm (blue)	Motor (yellow)	9.2	0.84	94–95, 106–107, 123–141, 590–594	P590, N591, I592, I593, R594
Lever (red)	Motor (yellow)	24	0.43	419–423, 433–440	L420, K421, T435, Y439

N-terminal subdomain (Nterm) includes residues 12–94; 107–129; 591; and 594–629. Lever includes residues 420–433; and 630–734. Motor includes residues 95–106; 141–419; 440–590; and 592–593.

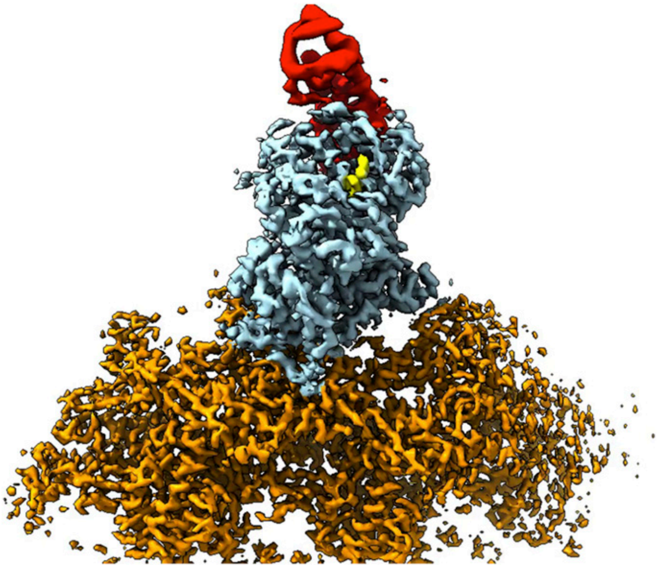

Movie S1. Overview of the AM.ADP^{A} map. Density for actin is rendered in orange, with myosin in pale blue or red for the lever arm. Nucleotide density (myosin active site) is rendered in yellow.

Movie S1

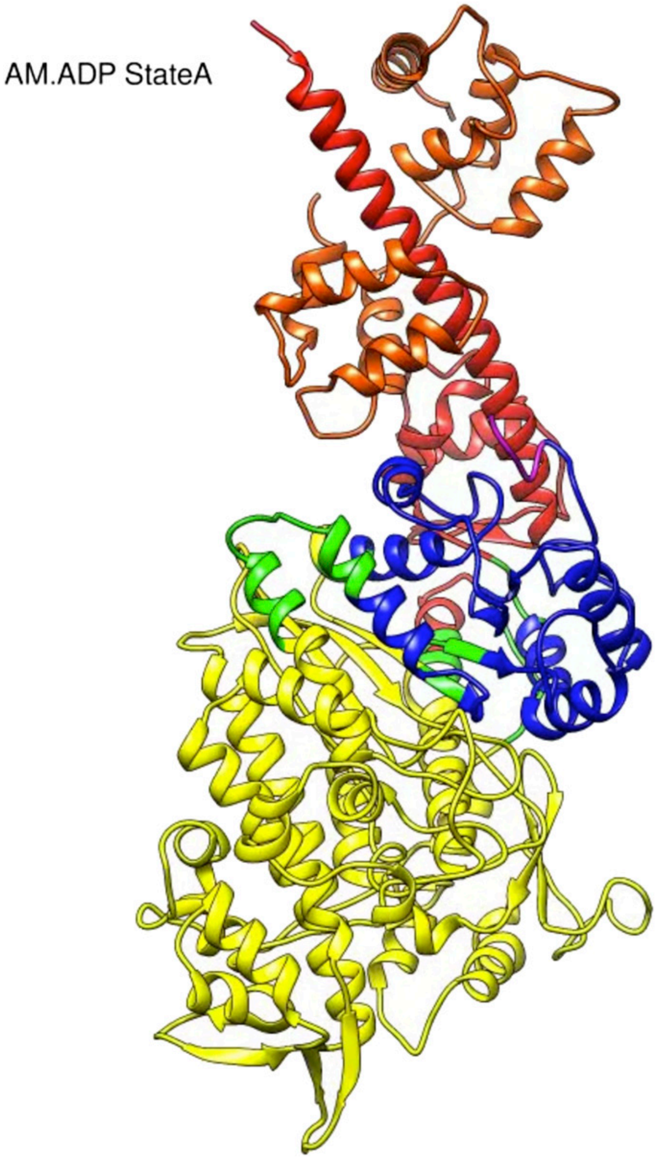

Movie S2. Structural changes in myo1b between AM.ADP^A, AM.ADP^B and AM states. Animation accompanying Fig. 1*A* by direct morphing the final fitted AM.ADP^A, AM.ADP^B and AM models. Whereas the actin binding site is basically unchanged (not shown in the animation), the N-terminal domain translates and rotates and the lever swings 24° (see Table S2 for subdomain orientations relative to a fixed domain defined by DynDom). Myosin coloring is based on DynDom subdomain definition; CaM is in orange red.

Movie S2

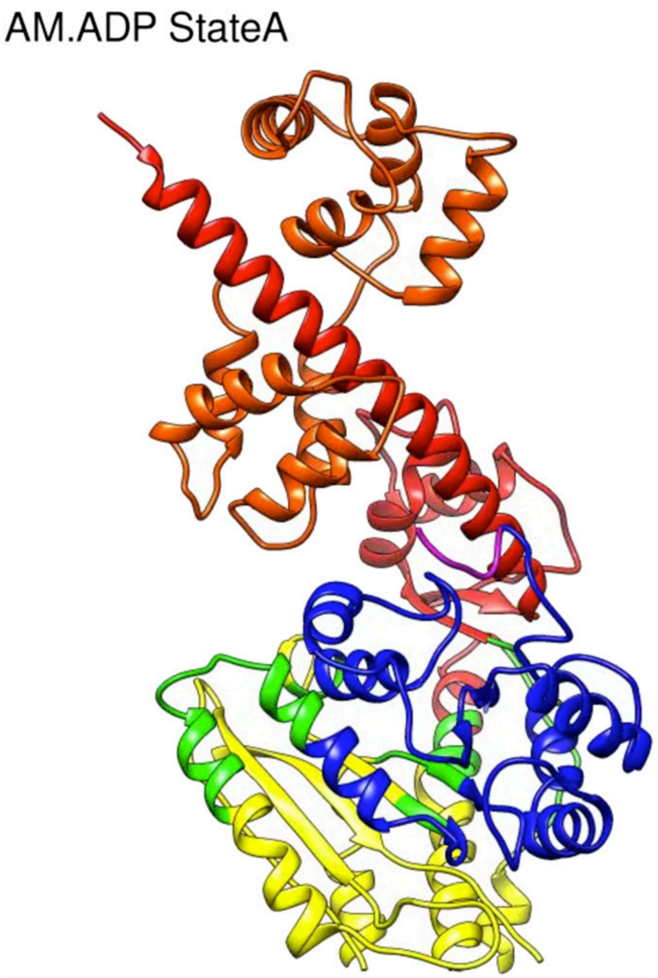

Movie S3. Close-up view of structural changes in the N-terminal subdomain and lever structural between AM.ADP^A, AM.ADP^B, and AM states. Animation accompanying Fig. 2 *A* and *B* by direct morphing the final fitted AM.ADP^A, AM.ADP^B, and AM models. The orientation of N-terminal subdomain (blue), 24° swing of the lever (red) and docking of the N-terminal extension (magenta) from AM.ADP^A to AM.ADP^B state are clearly seen in the animation. Myosin coloring is based on DynDom subdomain definition; CaM is in orange red, and bending residues are in green.

Movie S3

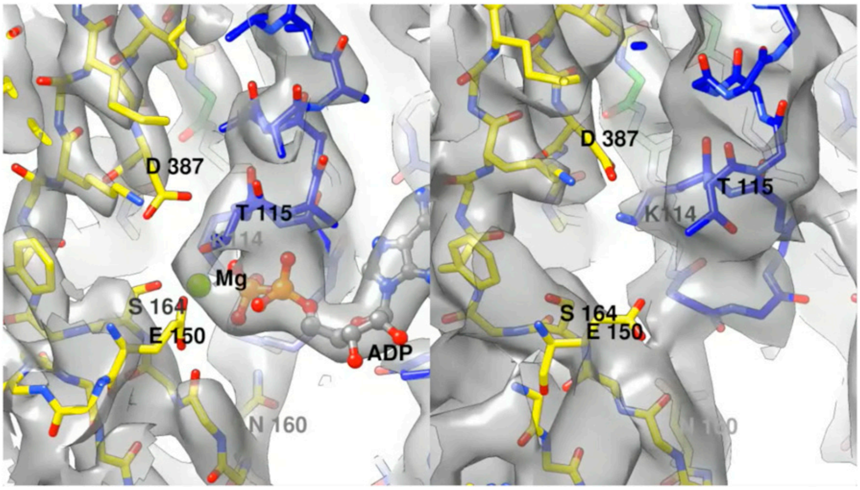

Movie S4. The AM.ADP^A active site. Animation accompanying Fig. 3 for nucleotide binding site of myo1b in the AM.ADP^A and AM states showing side-chain interactions with MgADP in the density.

Movie S4

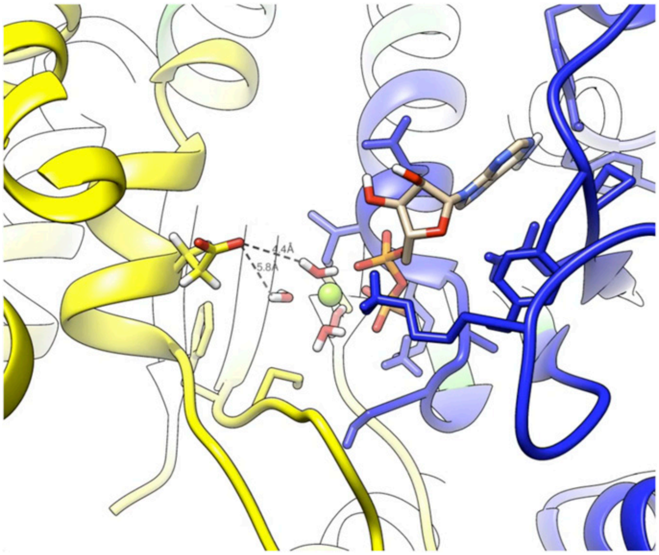

Movie S5. The coordination of residue E150 with the first water shell around the Mg atom during MD Flexible Fitting of AM.ADP^A structure into cryo-EM density. MD modeling suggests a transient interaction between the magnesium water shell and E150, a residue in the HH helix that is highly conserved across the myosin superfamily, but that has not been associated with a nucleotide interaction. Residues interacting directly or indirectly with MgADP and four water molecules are shown with sticks. Distance changes between E150 and two water molecules are labeled and shown with black-dashed line. Myosin coloring is based on DynDom subdomain definition.

Movie S5

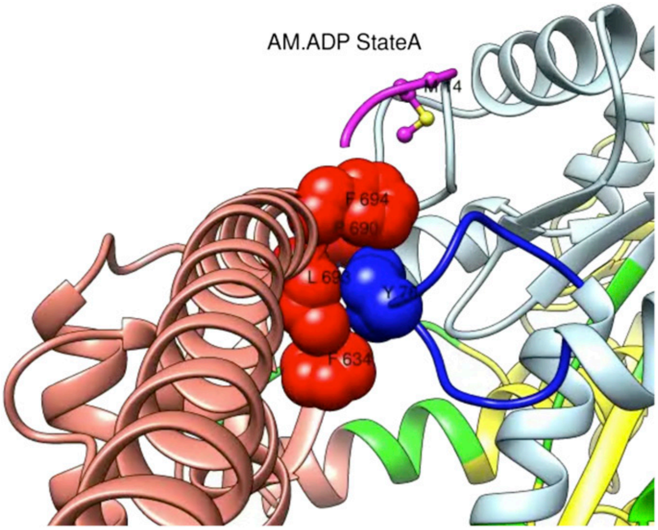

Movie S6. Interaction of loop 5, lever, and N-terminal extension between AM.ADP^A, AM.ADP^B, and AM states. Animation accompanying Fig. 2*C* by directly morphing the final fitted AM.ADP^A, AM.ADP^B, and AM models. The loop 5 (blue), orientation of the lever (red), and docking of N-terminal extension (magenta) from AM.ADP^A to AM.ADP^B and to AM states are clearly seen in the animation. Myosin coloring is based on DynDom subdomain definition.

Movie S6

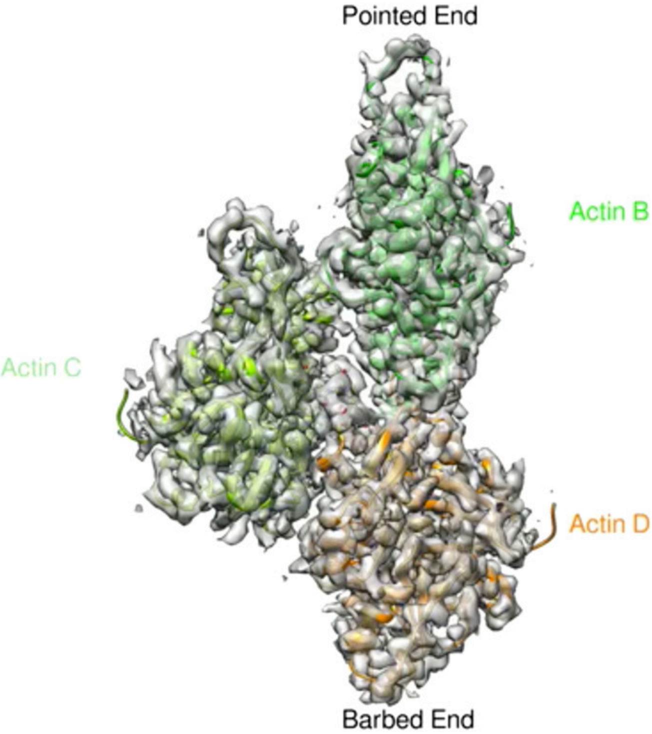

Movie S7. Phalloidin binding site on actin filament. Animation accompanying Fig. 5 showing phalloidin structure and its interactions with three actin subunits in AM.ADP^A state together with the cryo-EM density map. The phalloidin model and residues in three actin subunits [actin B (green), C (light green), D (orange)] interacting with phallodin are shown with stick, and four H-bonds between phalloidin and actin monomers as given in Fig. 5*B* are shown with yellow line.

Movie S7